Novel Image Analysis Method for Blade Aerodynamic Performance on Operational Turbine

Nigel Swytink-Binnema, David A. Johnson
Wind Energy Group, Department of Mechanical Engineering, University of Waterloo, 200 University Avenue West, Waterloo, ON N2L 3G1, Canada

E-mail: nswytink@uwaterloo.ca, da3johns@uwaterloo.ca

Abstract. Tuft flow visualisation has been used to study aerodynamic stall on wind turbine blades for several decades. In recent years, advances in the processing power of personal computers have made digital image processing vastly more accessible. In this paper, therefore, a novel method is presented to digitally analyse tuft flow visualisation on the blade of an operating wind turbine. Examination of the outboard 40% of the blade of a 10 m diameter wind turbine revealed stalled flow in wind speeds from 5 m/s to 20 m/s. The region of stall at those speeds increased from 5% to 40% of the coverage area of the tufts. This increase in the amount of stalled flow is expected for stall-regulated wind turbines. Overall, the results are very promising and demonstrate potential for a wide range of aerodynamics applications including real-time blade stall determination and classical wind tunnel aerodynamics studies.

1. Introduction

Aerodynamic stall in a dynamic airflow produces unpredictable loads on the blades of wind turbines making the structural design of the blades more difficult. Therefore, flow visualisation methods such as tuft visualisation have been used to study the phenomenon of wind turbine blade stall. There are many variations on the tuft method, including tuft grids, surface tufts, and mini-tufts [1, 2, 3], and therefore the types of results produced also vary. More subtly, the interpretation of the results also depends on the setup and assumptions of the researchers.

Conventional tuft flow visualisation on a wind turbine requires the installation of tufts on the blade either: in an outdoor study in a time period of relatively steady wind velocities (both magnitude and direction) [4, 5, 6, 7]; or in a wind tunnel [8, 9]. A camera records the tuft images for manual inspection at a later time. The methodology used for a small subset of such studies is discussed below.

Pederson & Madsen [4] compared the observed location of the separation line from tuft video with a numerical code. After recording one hour of video, 5 rotor revolutions (comprising 8.5 s of imagery) were analysed in detail and one particular revolution with a 0° yaw offset provided the best agreement with the code. Limited camera resolution prevented viewing of the tufts near the tip, and the authors described significant difficulty in determining clear trends from the video. No mention was made of the criteria used to determine the separation line.

Eggleston & Starcher [5] examined the stall characteristics of three downwind wind turbines with diameters in the range of 6.3 m to 13.5 m using a boom-mounted camera projecting from the hub perpendicular to the rotor plane. The exposure time on the camera was set to a value at which the tufts would blur when "vibrating rapidly." Analysis of the centrifugal forces on

individual tufts showed that tufts which were lifted from the surface or oriented significantly away from the flow direction could be considered stalled. Flexible filaments have been shown to oscillate under certain conditions [10], yet it is not clear exactly what amount of tuft blurring or what tuft angle corresponds to stalled flow in Eggleston & Starcher's study. As in the study by Pederson & Madsen [4], Eggleston & Starcher note the insufficient resolution at the blade outer region where a higher fraction of the mechanical power is produced.

Maeda & Kawabuchi [7] used tuft visualisation to complement a pressure-based study of a 10 m diameter wind turbine in yawed flow. Once again, however, there was limited resolution at the blade tip. In order to record the suction surface of the blade, the camera was mounted on a short boom projecting towards the nacelle side of the rotor. This configuration resulted in a very small viewing angle for the camera yet the authors were able to locate a region of full stall. In personal correspondence with the principal author, however, washout due to the position of the sun was said to have played a significant role in limiting their results.

In a wind tunnel study described by Haans *et al.* [8], a camera was placed downwind of a 1.2 m diameter wind turbine fitted with tufts. A strobe light was synchronised to the blade passage in order that the rotor appeared stationary. Unlike the typical video method, the blade made a full rotation before another image was taken. This is significant because it resulted in a dataset which was uncorrelated in time: no measure of oscillation may be made between one image and the subsequent one. The authors reasoned, therefore, that only tufts oriented in a purely radial direction indicated stalled flow.

A major disadvantage in all these studies is that uncharacteristically steady winds are required to form some type of conclusion about the blade stall. Further, in the case of outdoor tests, researchers manually review video to locate a particular instance with notable trends. This has the potential to introduce significant bias to the results if, on average, there is in fact no significant trend. Yet outdoor studies are still necessary since the highly controlled conditions—typically with small models—in wind tunnels (and even more so in numerical models) only yield conclusions about the specific wind conditions studied.

In Pederson & Madsen [4], the authors stated that manual interpretation of the video "was rather time consuming" and that digital image processing "was discussed, but not tested." They conclude that the video evaluation techniques "must be further developed." In the intervening decades, high definition digital image capture, digital storage, and digital processing have all become vastly cheaper and faster. In the present paper, a novel digital image processing method is presented which calculates the fraction of stalled flow on a blade from tuft video on an operating wind turbine. The focus will remain on the details and validation of the method; a brief look at the results follows at the end.

2. Experimental setup

The 10 m diameter horizontal-axis wind turbine shown in Figure 1 was used in this study. It is situated at a field test site on a small hill beside a bank of trees to the northeast (site coordinates: 43.5°N, 80.5°W, 400 m elevation). The wind rose is highly biased towards the northwest and the trees have no discernible effect on the wind profile in that direction [11]. The specifications of the Wenvor 30 wind turbine are given in Table 1.

A model 05103 RM Young propeller anemometer with vane is located at 20 m elevation on the turbine tower and an NRG #40C cup anemometer is situated at 10 m elevation. With True North at 0°, the dominant wind direction is in the 240° to 330° range, which was also previously found to have the lowest terrain roughness [11]. Based on 120 h of data in the dominant wind direction, the wind shear exponent (in that direction) is 0.25.

One hundred and one 4 cm long tufts of 2.5 mm black acrylic yarn were fixed to the suction surface of one of the blades with transparent Scotch Tough Duct Tape. In the layout pattern shown in Figure 2, the spanwise separation was 12 cm and the chordwise separation was 8 cm

Figure 1: Wenvor 30 turbine and met tower.

Table 1: Details of Wenvor 30 turbine.

Power	25 kW at 15 m/s
Diameter	10 m
Design	upwind
Blades	2
Rotor speed	120 rpm
Tip pitch	3°
Blade twist	0°
Blade taper	elliptical
Yaw control	passive
Hub height	31 m

or 10 cm measured relative to the quarter chord. A GoPro HERO2® high definition (HD) camera is shown in Figure 3a installed with the lens centreline tilted 14° towards the blade at a radial position of $0.11R$ on the tufted blade of the turbine. This camera had several advantages including: wireless control and video retrieval, HD picture recorded at 30 Hz, fixed lens (aiding image stability), and a design for outdoor use at an extended temperature range.

The original 1080×1920 pixel video shown in Figure 3b was cropped to 160×240 pixels representing the outer 40% of the blade ($r/R \geq 0.6$) as shown in Figure 3c. This reduced processing time and digital storage space significantly. Further, lens distortion from the 90° wide-angle lens which distorted the edges of the image shown in Figure 3b was negligible in the cropped image in Figure 3c. Finally, most of the mechanical power is produced in the outer portion of the blade, so the choice to limit analysis to that section was expected to yield valuable results. In general, 48 of the original 101 tufts were visible in the cropped image.

3. The algorithm

As in the study by Haans *et al.* [8], each image from the video was processed separately from the others. This required two distinct processes: locating tufts; and determining which of those were "stalled" (i.e. were indicating stalled flow).

3.1. Inputs to algorithm

Three inputs were required for the algorithm: the tuft image (Figure 4a), a background mask (Figure 4b), and the location of the tuft anchor points (Figure 4c). Since the blades flex depending how much aerodynamic load they experience, a set of eight masks and corresponding set of eight tuft anchor points were prepared. These correspond to the flex position N, where

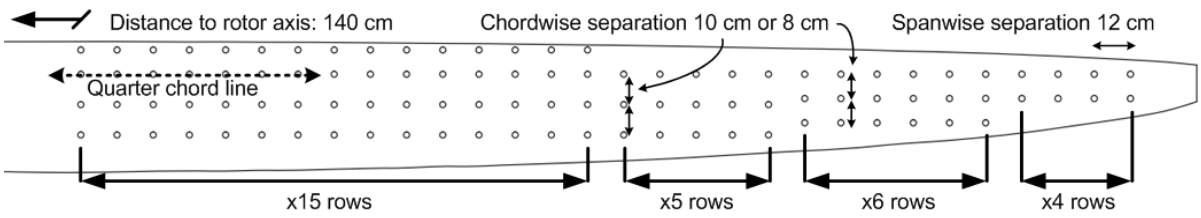

Figure 2: Layout of 101 tufts on blade (anchor points shown by circles). Top is leading edge. Camera located left of image, 85 cm from first tufts.

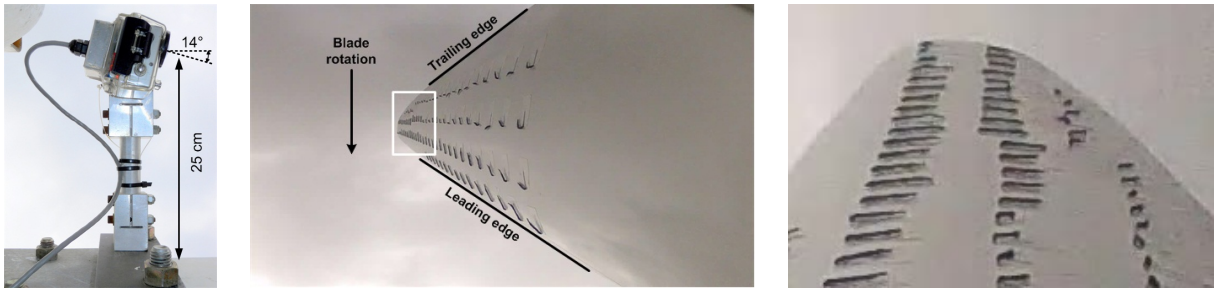

(a) camera (b) 1080 × 1920 pixel original image (c) 160 × 240 pixel cropped image

Figure 3: GoPro® camera installed on blade at $0.11R$ with 14° tilt produces the images shown.

$N = 1$ is the lowest amount of flexure. The mask and anchor images were shifted upwards in increments of 10 pixels to the highest flexure at $N = 8$ (small adjustments to the shapes were made based on a review of the video). The sample images in Figures 4b and 4c correspond to a blade flex position of $N = 5$.

3.2. Locating tufts

Three main steps were required to locate tufts in the image and were completed with image processing code written for MATLAB®. These steps are outlined below as applied to the example image in Figure 4a:

Step 1: The image was converted to black & white (B&W) as shown in Figure 5a. This was done by applying the background mask at the lowest intensity of the greyscale image (pure black in this example), maximising the contrast using a built-in MATLAB® function, and converting the greyscale intensity values to black or white pixels based on a threshold value also automatically determined by MATLAB® functions.

Step 2: The foreground of the image was extracted by removing any black regions touching the edges. The result for this example is shown in Figure 5b.

Step 3: Of the remaining regions, those identified as tufts were kept and are highlighted in black in Figure 5c for this example. The paragraph below provides a description of how this was accomplished.

In order to determine which black regions were tufts, algorithms were developed and implemented to determine the area, extrema, and eccentricity for each region in Figure 5b. Any region whose area was within the range of 8 to 150 pixels may be considered a tuft: the

(a) Input 1: greyscale image (b) Input 2: background mask (c) Input 3: tuft anchors

Figure 4: Inputs to algorithm.

(a) Step 1: convert to black & white (b) Step 2: extract foreground (c) Step 3: tufts located

Figure 5: Algorithm steps to locate tufts.

large range was necessary because of parallax effects at the low (14°) camera angle. The second criterion was that at least one of the outer extremities of the region must lie on the tuft anchor lines from Figure 4c. The tuft anchor lines were designed to account for some amount of camera and blade vibrations while minimizing the chance of coinciding with the free end of a tuft. The design is imperfect as seen by the two tufts in the central line of Figure 5c which are incorrectly discarded. The final criterion was that the elliptical eccentricity of "an ellipse that has the same second-moments as the region" [12] must be at least 0.8 implying that $\frac{b_2}{b_1} \leq 0.6$. Here, b_1 and b_2 are, respectively, the lengths of the major and minor axes of the ellipse. Without this final criterion, if the tuft appeared too circular the algorithm would not be able to reliably determine the angle of the tuft—and hence whether it was stalled—based on the angle of its representative ellipse.

The number of regions remaining (41 in Figure 5c) was defined as n, the number of tufts located. In order to calculate the flex position N, the following equations were used:

$$N_k = N_j + \sum_{i=0}^{k-1} i \times (-1)^i \qquad 1 \leq k \leq 15 \tag{1}$$

$$N = N_k \qquad 1 \leq N_k \leq 8 \tag{2}$$

Beginning with N_j—the flex position from the previous image—k attempts were made to choose the flex position. The final N used was the N_k at which either: the maximum number of tufts was located; or the number of tufts located was at least $n_{\min} = 35$ (whichever occurred first as k was increased). While a total of 48 tufts were visible in the images, a dependence study determined that increasing $n_{\min}$ above 35 yielded no visible improvement in the final results while significantly increasing the processing time; hence, $n_{\min} = 35$ was used for the threshold in all subsequent analyses.

3.3. Locating stalled tufts

As in studies by other researchers, the tuft angle was the primary method used to determine if a tuft was in stalled flow. Three angles may be defined to indicate stall corresponding to angles δ_{L}, δ_{R}, and δ_{IP} in Figure 6. δ_{L} is the degree to which the tuft is lifted from the surface of the blade; any nonzero value for δ_{L} should indicate stall in a low-pressure region. δ_{R} is the radial deflection of the tuft due to the ratio of centrifugal forces to aerodynamic forces on the tuft. δ_{IP} is the angle of the tuft with respect to the horizontal in the image plane. Unfortunately, while δ_{IP} is the only angle which may be measured by the algorithm, it is a combination of δ_{L}, δ_{R}, the camera viewing angle $\delta_{\mathrm{tilt}} = 14°$, lens distortion, and the blade profile curvature at that point δ_{B}.

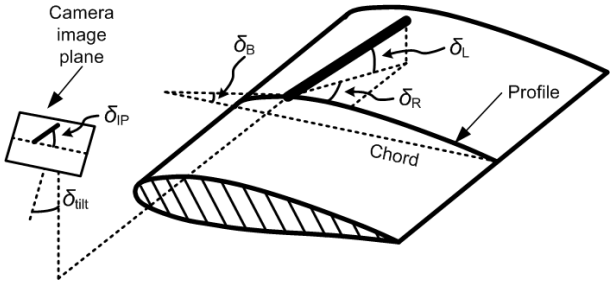

Figure 6: Angles which contribute to apparent tuft angle.

Since the image plane was nearly parallel to the blade profile cross-section, the blade profile curvature at each tuft anchor point was assumed to represent the angle of a tuft in fully attached flow. The profile curvature varied from $-13°$ to $+9°$ at the tuft anchor points. As an estimate of stall, therefore, any tuft in the image with an angle outside the range $\pm 13°$ was considered to be in stalled flow. Even with this value, it is possible for a tuft in the lower left corner of the image to have a 13° angle yet be in fully attached flow. Conversely, it is possible for a tuft to have a 0° angle in the image with $\delta_R = 60°$, in all likelihood indicating stalled flow. This is not so much a difficulty with the algorithm as it is with the method of tuft flow visualisation with a low camera viewing angle; as mentioned previously, to the authors' knowledge, no other researcher has discussed what precise criteria are used to extract stall-related parameters such as the separation line from tuft flow video.

The tuft angle was estimated with the orientation angle of the tuft equivalent ellipse shown in Figure 7a. This example is a magnification of the bottom right tuft in the example image (Figure 5c) and individual pixels are visible. Due to the angle range of $[-90°, 90°]$, however, this criterion only accounts for the unshaded regions in Figure 7b. Upstream-pointing tufts were accounted for by the "upstream zone" in Figure 7b which describes cases whereby a right extremum lay on the anchor point while a left extremum did not. The tufts which met this criterion are highlighted in Figure 8a while those which met the first ($|\delta_{IP}| > 13°$) criterion are highlighted in Figure 8b. Note that some tufts satisfy both measures of stall yet only one was required to tag any particular tuft.

3.4. Stall fraction

From the number of stalled tufts (Figure 8) and the total number of tufts located, n, the stall fraction ζ may be calculated:

$$\zeta = \frac{n_s}{n} \tag{3}$$

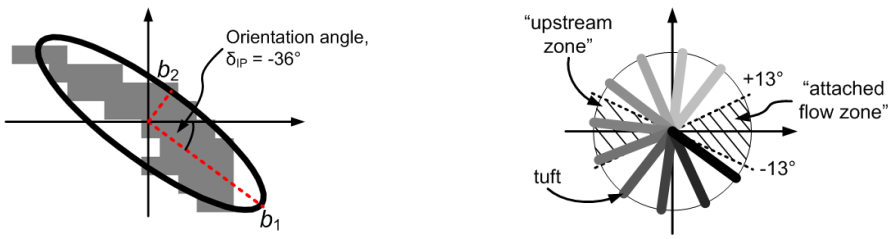

(a) sample tuft angle δ_{IP} (b) possible tuft angles

Figure 7: Tuft angles which determine if tufts are interpreted as "stalled."

(a) tufts pointed upstream (b) tufts at high angle

Figure 8: Algorithm location of stalled tufts.

where n_s is the number of tufts tagged as "stalled." The stall fraction ζ has the following two important characteristics:

(i) It is dependent on n: the higher the number of tufts located, the higher the precision of ζ and the more statistically reliable the estimate is.

(ii) It refers to only the outer 40% of the blade. The fraction of the entire blade which is stalled will therefore be higher given that the general trend seen when reviewing video was for the stall to progress from the inboard to outboard sections.

The final image produced by the algorithm is shown in Figure 9 with $\zeta = 0.24$: the background mask and tufts are shown in grey except for stalled tufts which are black. The original greyscale image first shown in Figure 4a is included again for comparison. The steps outlined in Sections 3.1–3.4 were applied to each frame of the cropped video; only N was carried forward to the subsequent frame (N_j in Equation (1)). In this manner, each full-colour frame of the video was condensed to three numbers: ζ, n, and N. This represents a vastly reduced dataset size and yields the potential to easily calculate statistics and relations between these and other parameters such as velocity or power.

3.5. Validation

In order to determine the overall validity of the stall fraction ζ returned by the algorithm, the amount of stall was manually estimated for a subset of the images. 388 images were randomly selected with the stipulation that there be an approximately uniform distribution of stall from $\zeta = 0$ to $\zeta = 1$. For each image, the number of stalled tufts was recorded and divided by 48, the number of tufts visible in a typical image. In order to qualify as "stalled," similar criteria as those of the algorithm in Section 3.3 were applied except that: (a) the tuft angle

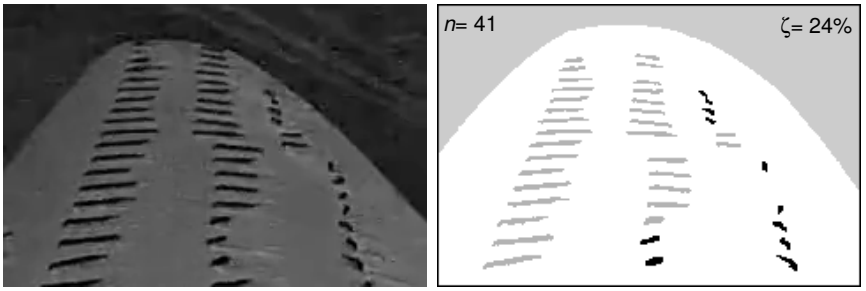

Figure 9: Final tuft image output from algorithm compared with original input.

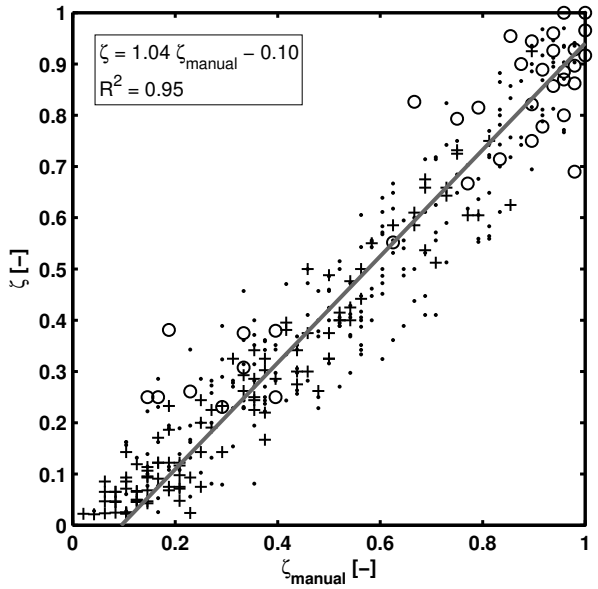

Figure 10: Bias error of algorithm. Of 388 points: 36 have $n < 30$ ($\circ$); 241 have $30 \leq n < 40$ ($\bullet$); and 111 have $40 \leq n < 50$ (+). Linear regression is shown for the 352 points with $30 \leq n < 50$.

δ_{IP} was not measured but rather approximated; and (b) tufts which may be discarded as too circular were nonetheless included. This provided an estimate of the bias error and the spread of data due to algorithm functions such as the greyscale contrast optimization, B&W conversion, tuft anchor positions, blade masks, and so on. The 388 manually-obtained stall fractions and corresponding estimates from the algorithm are plotted in Figure 10 separated according to the number of tufts located. Recall that higher values for n provide more reliable estimates for ζ. Of these 388 images, 352 (91%) have $n \geq 30$. Most points in the figure with $n < 30$ occur at higher ζ, likely due to a combination of factors: tufts oriented perpendicular to the image plane in stalled flow appear as circles and are discarded based on their low eccentricity; there were several cases of extreme blade flex which even the $N = 8$ position could not accommodate; and higher amplitude vibrations during high stall events may cause many tufts to move outside the bounds of the fixed-width anchor lines of Figure 4c. Using data with $n \geq 30$ only, therefore, the total least squares linear regression which relates the two stall fractions is:

$$\zeta = 1.04\zeta_{\mathrm{manual}} - 0.10 \tag{4}$$

where ζ_{manual} is the manually-obtained stall fraction. This regression used the total least squares method [13] which minimizes the perpendicular distance to the line. The line, shown in Figure 10, lies below the line $\zeta = \zeta_{\mathrm{manual}}$ at all points. This slight negative bias was expected for two reasons: first, vibrations of the camera and blade occasionally cause momentary excursions of some tufts from the predicted tuft anchor points (while the human eye can account for this, the computer cannot); and second, when a tuft is pointing in the radial direction, it may appear to merge with the one at the next radial position as may be seen in two trailing edge tufts in Figure 9 (top-right of image). The occurrence of this would decrease the number of tufts located since a single black region would comprise multiple tufts: by subtracting 1 from the numerator and denominator of Equation (3), the result is a decrease in the stall fraction (since n is greater than n_{s}). The same effect occurs for tufts which are oriented nearly perpendicular to the image plane and discarded for appearing too circular. Note that a threshold stall angle of 25° instead of 13° resulted in a significantly lower slope of 0.88 in Equation (4). The correlation coefficient of 0.95, Equation (4), and the 91% of images with $n \geq 30$ in Figure 10 all suggest that the algorithm performs as it was designed using a 13° threshold angle.

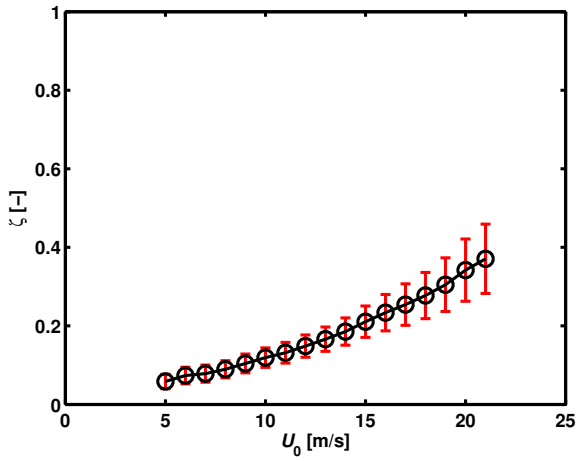

Figure 11: Binned ζ–U_0 curve for May 12.

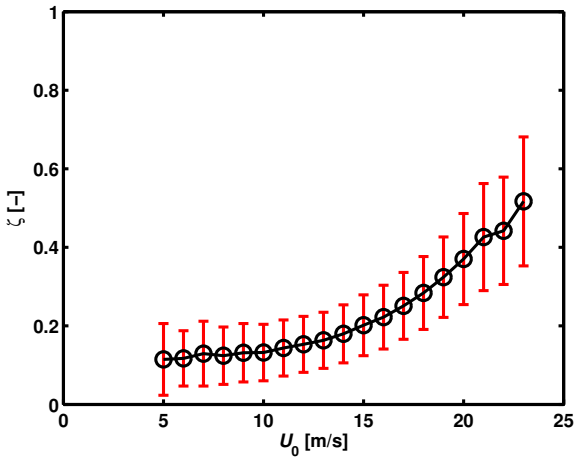

Figure 12: Binned ζ–U_0 curve for Nov 1.

4. Results

4.1. Data reduction

Data from the 20 m anemometer and the camera were time-synchronised to within 1 s using the clock on the PC on site. The power law exponent of 0.25 was applied to relate the wind speed measured at 20 m on the wind turbine to the hub height wind speed. The following three filters were imposed on every second of data: the turbine must be producing electrical power; the wind direction measured at 20 m on the turbine tower must be between 240° and 330°; and the number of tufts located must be $n \geq 30$. The data that remained comprised the primary data set for any data campaign.

4.2. Stall fraction

Tuft video presented here was recorded on two days in 2013: May 12 and November 1. Each data campaign comprised 3.5 h (approximately 375 000 images) of relatively high average wind speeds in order to record the full range of input conditions. The statistics from each day are presented in the table below:

Date (y/m/d)	Total Images	Total after filters	$\overline{U}_0$	σ_U	$\overline{P}$	σ_P
2013/05/12	376 226	350 586 (93.18%)	11.7 m/s	2.7 m/s	22.2 kW	9.6 kW
2013/11/01	374 143	277 009 (74.04%)	13.6 m/s	3.0 m/s	25.2 kW	8.2 kW

1 s averages were calculated from the 30 Hz data in order to synchronize this with the 1 Hz velocity data. Bins with at least 10 s of data are plotted in Figures 11 and 12 for, respectively, the May 12 and November 1 data sets. The error bars represent the root sum of squares of the bias and precision errors: bias error was derived from the difference between the actual number of tufts in the image and the average number located by the algorithm; precision error was the typical two standard deviations from the mean of each bin divided by the square root of the number of points. Each bin from 7 m/s to 19 m/s contained over 100 s of data and each bin from 10 m/s to 15 m/s contained over 1000 s of data.

The first major trend visible from the plots in Figures 11 and 12 is the increase in stall fraction with wind speed. This was expected for this stall-regulated wind turbine and shows that the algorithm holds tremendous promise for more in-depth investigations. The curves overlap one another well within the uncertainty. It is interesting to note the difference in the size of the

uncertainty in each data set. At all wind speeds, the uncertainty in the May 12 data is much lower: this is most visible at the lowest wind speeds, for example at 5 m/s where the uncertainty is ± 0.02 on May 12 but ± 0.10 on November 1. An average of 34 tufts out of 48 were located on November 1 whereas on May 12 the average was 41. This is likely due to the video quality: the images from November 1 were more blurred and had fewer discernible tufts than May 12. By November 1, the camera enclosure's lens cover was no longer fully transparent and a few of the outer tufts were torn off likely due to the rain that day. The high uncertainty values from November 1 quantifiably reinforce the value of quality high definition tuft video (as in May 12) in analysing wind turbine blade stall.

5. Conclusions

A digital image processing algorithm was presented which calculates the amount of stall from tuft visualisation on the blade of an operational wind turbine. When given an image with minimal lens distortion and knowledge of the anchor points of tufts installed on the blade, the algorithm achieved a bias error better than -10% compared to manually-estimated stall.

The method was successfully applied to seven hours of tuft video on a 10 m diameter stall-regulated wind turbine. On the outboard 40% of the blade, the fraction of tufts revealing stalled flow increased from 5% to 40% as the wind speed was increased from 5 m/s to 20 m/s.

Overall, the results are very promising and demonstrate good agreement with the expected behaviour for a stall-regulated wind turbine. While the application was presented for post-processing of video from a field-installed wind turbine, the method holds potential for a wide range of aerodynamics applications including real-time blade stall determination for pitch control as well as for more classical wind tunnel aerodynamics studies. Future work may also include azimuthal variation of the stall.

Acknowledgments

The authors wish to acknowledge support from the Natural Sciences and Engineering Research Council of Canada and the Ontario Centres of Excellence and thank Nicholas Tam and Curtis Knischewsky at the University of Waterloo for their invaluable contributions to instrumentation.

References

[1] Crowder J P 1989 *Handbook of Flow Visualization* ed Yang W J (Hemisphere Publishing Corporation) chap 9, pp 125–175
[2] The Japan Society of Mechanical Engineers 1988 *Visualized Flow: Fluid motion in basic and engineering situations revealed by flow visualization* 1st ed (Toronto, ON: Pergamon Press)
[3] Mabey D, Welsh B and Pyne C 1995 *Aeronautical Journal* **99** 178–182
[4] Pederson T F and Madsen H A 1988 *Wind Energy Conversion: Proceedings of the 1988 tenth BWEA wind energy conference* ed Milborrow D (London: Mechanical Engineering Publications Ltd) pp 155–162
[5] Eggleston D and Starcher K 1990 *Journal of Solar Energy Engineering* **112** 301–309
[6] Bruining A 1994 *EWEC 1994 Conference Proceedings* (Thessaloniki, Greece) pp 675–480
[7] Maeda T and Kawabuchi H 2005 *JSME International Journal Series B* **48** 156–163
[8] Haans W, Sant T, van Kuik G and van Bussel G 2006 *Journal of Solar Energy Engineering* **128** 472–480 ISSN 01996231
[9] Armstrong S, Fiedler A and Tullis S 2012 *Renewable Energy* **41** 13–22 ISSN 09601481
[10] Zhang J, Childress S, Libchaber A and Shelley M 2000 *Nature* **408** 835–839 ISSN 0028-0836
[11] Lam V 2013 *Development of wind resource assessment methods and application to the Waterloo region* MASc University of Waterloo (Available from `http://hdl.handle.net/10012/7604`)
[12] The Mathworks Inc 2013 Documentation Center (accessed 19 November 2013 from `http://www.mathworks.com/help/documentation-center.html`)
[13] Krystek M and Anton M 2007 *Measurement Science and Technology* **18** 3438–3442 ISSN 0957-0233